EXPERIMENTAL STUDY OF IMPURITY PRODUCTION

IN THE TOKAPOLE II TOKAMAK

by

NANCY SUSAN BRICKHOUSE

A thesis submitted in partial fulfillment of the

requirements for the degree of

DOCTOR OF PHILOSOPHY

(Physics)

at the

UNIVERSITY OF WISCONSIN-MADISON

1984

EXPERIMENTAL STUDY OF IMPURITY PRODUCTION

IN THE TOKAPOLE II TOKAMAK

Nancy Susan Brickhouse

Under the supervision of Professor Richard Norman Dexter

Impurities are introduced into tokamak plasmas by plasma bombardment of the surfaces, particularly in the presence of large sheath potentials. Since these impurities can grossly affect the plasma behavior, understanding and control of the production mechanisms are crucial to the achievement of clean discharges. Results of a study of impurity production on Tokapole II, a tokamak with a four-node poloidal divertor, are reported.

The release mechanism for low-Z impurities in Tokapole II has been characterized through impurity doping and isotopic exchange experiments. The desorption mechanism responsible for the low-Z impurity concentrations during the rise phase of the plasma current depends on the mass of the plasma ions. Doping with small amounts of any gas studied (H_2, D_2, He, N_2, O_2, Ne, Ar, Kr, and Xe) increases the early-time radiation of O, C, and N. For exotic gas doping this increase is linear with the dopant concentration, and proportional to the mass of the dopant, as expected for a momentum

transfer process. Isotopic exchange experiments confirm the mass-dependence of oxygen production.

A time-dependent coronal model is compared with the vacuum ultraviolet spectroscopic signals of the ionizing oxygen. The quantity σ/τ (desorption cross section divided by particle confinement time) is determined to be $4 \times 10^{13} cm^2/msec$. The oxygen influx has a large peak early in the start-up.

The ion-induced desorption is consistent with the edge potential and temperature measurements. These measurements indicate that the sputtering of aluminum during start-up should be negligible, as is observed. Instead aluminum is probably due to unipolar arcing; copper production is a combination of processes.

The recycling of impurities during the steady-state phase is discussed. Since the start-up phase is particularly active in producing impurities, and since the recyling impurities can be more effective than hydrogen in further production with their higher mass and charge, control of the start-up is important for impurity reduction.

ACKNOWLEDGEMENTS

I would like to thank my major professor, Richard N. Dexter, for his encouragement of this research project and for his sustained confidence in me. I appreciate the time he has spent and the useful criticisms he has made.

I thank Professors Clint Sprott, Stewart Prager and Jim Callen for discussions and suggestions in my research.

The technical crew on the Tokapole have provided the invaluable service of keeping the equipment operational. In particular, Tom Lovell's advice and general curiosity have helped to make the laboratory experience interesting. I thank Kay Shatrawka for her help in the production of this manuscript.

I am enormously grateful to my fellow graduate students. Don Holly, Arnie Kellman, Alan Biddle, Doug Witherspoon, and Dave Shepard have all given advice and encouragement. I thank Rich Groebner for doing the initial experiments in this area and for writing the thesis which has guided me through much of this work. In particular, I would like to thank Tom Osborne, who has spent many productive hours in discussion with me, and who has maintained a strong sense of doing physics properly. My collaboration with him has been a rewarding experience.

I would like to thank my parents, Mr. and Mrs. Robert Brickhouse, and other family and friends who have stood by me through my graduate career.

Finally, I thank my husband Andrew Szentgyorgyi for his love, understanding, and friendship. His enthusiasm for physics and for other pursuits has been inspiring.

Financial support has been provided by the United States Department of Energy.

TABLE OF CONTENTS

CHAPTER 1

INTRODUCTION

A. Overview of the Impurity Production Problem in Tokamaks

The working gas of present-day tokamaks provides a source for the desorption of low-Z (light) impurities and the sputtering of metal (heavy) impurities. Many possible mechanisms for introducing impurities are being studied: ion, electron, neutral, and photon induced desorption, thermal desorption, and chemical reactions to release light impurities, and evaporation, sputtering, blistering, and arcing to release metal impurities.[1]

Unipolar arcing and ion (or charge exchange neutral) sputtering are the major mechanisms for metal production in modern tokamaks. Usually arcing dominates during the start-up, while sputtering dominates during the steady-state.[2] The importance of the sheath potential between the plasma edge and the wall has been demonstrated both for arcing[3] and for sputtering.[4] The important mechanisms for light impurity production have been less well known experimentally. From theoretical considerations and from surface bombardment experiments in controlled environments, the dominant type of desorption for the relevant mass and energy ranges in a tokamak should be desorption induced by ions or charge exchange neutrals.[1,5]

After one to ten energy confinement times, the working gas may leave the central plasma region and reach the wall, where many processes may occur. Pumping by the wall (due to diffusion of the more energetic particles into the bulk solid) may cause a significant particle loss from the system. During the initial ionization phase, nearly half of the original filling gas is lost. In fact additional gas puffing throughout the discharge is necessary to maintain a steady-state electron density.[1] The early impurity build-up during this time of poor confinement indicates that there is a strong interaction with the wall. The working gas ions may knock adsorbed species from the wall or may reflect back towards the plasma. The series of processes by which plasma ions leave the plasma region, interact with the wall, and return to the plasma, through pumping, reflection, and desorption of additional working gas atoms is commonly referred to as recycling.

The relative importance of impurity recycling is not well understood. Potentially a small fraction of impurities may be a strong source of other impurities relative to hydrogen because of their larger mass and higher charge state, particularly if accelerated by a large sheath potential. A local density measurement of fully stripped oxygen on PDX has shown recently that the density of these highly charged ions at the limiter may be roughly 10% of their central density.[6] The energy of the ions hitting surface probes in the edge of PLT[7] and TFR[8] has also been found to be well above the expected ion temperatures based on the

electron temperatures there. The comparison between light and heavy impurity concentrations with concurrent measurements of the edge electron temperature under a variety of discharge conditions has given a qualitative understanding of ion sputtering in a tokamak. The presence of light impurities can contribute significantly to increased heavy impurity concentrations, as demonstrated on JFT-2;[9] however, on other machines, such as PLT, increased gas puffing cools the edge, reducing the energy of the bombarding ions, and thus reducing the heavy impurity concentration.[10] Models of the edge processes[11,12,13] account for both of these effects and for the relatively constant level of heavy impurities during a discharge. Working gas ion (and charge exchange neutral) sputtering is an important source;[14] nevertheless, a small percentage of light impurity ions can dominate the sputtering by two effects. Their larger mass gives them a larger momentum transfer to the wall for a given energy. Also, the multiply charged ions can gain more energy in the sheath potential. The impurity ions can thus cause an increase in sputtering, but only up to the point at which their radiative cooling of the edge reduces the sheath potential. Typical sheath potentials are on the order of sputtering thresholds, so that this edge cooling could actually eliminate sputtering.

Much progress is being made in understanding the details of these edge processes. Many machines are now making measurements of the relevant edge parameters.[15] Meanwhile, theoretical models for edge plasma transport, including atomic and molecular processes, the

plasma-wall interaction and impurity production mechanisms, and the particle flow with respect to boundaries such as limiters and divertors, are contributing to a comprehensive understanding of the edge physics.[16]

The deleterious effects of the plasma-wall interaction in a fusion reactor have been discussed at great length. The damage to reactor walls due to plasma and radiation bombardment and thermal load is of serious concern. Experiments at Columbia University were designed to simulate the effects of bombardment by a warm deuterium plasma on first wall material candidates. The plasma was given the energy flux expected at the first wall during one year of operation of a tokamak reactor. The materials tested showed blistering, melting, cracking, embrittlement,[17] and unipolar arcing.[18] The crucial problem to the fusion reaction itself is, of course, the ability of a small percentage (0.2 % tungsten) of partially stripped high-Z impurities to radiate all of the input energy, and thus prevent ignition.[19] Additionally, the start-up phase of a large tokamak such as TFTR must be designed to minimize the deleterious effects of low-Z as well as high-Z impurity radiation.[20]

In present tokamaks, impurities modify the density and temperature profiles not only by radiating power but also by adding electrons from multiply stripped ionic states, increasing the plasma resistivity, and altering transport processes. These effects in turn may alter the plasma stability behavior. The improvement in energy confinement with increased impurity levels (non-gettered

discharges) on ISX-B has been reported.[21] Divertor tokamaks with neutral beam heating have observed two new types of instability recently. Edge relaxation phenomena occurring during the H-mode, first reported by the ASDEX team, have been associated with high edge temperatures.[22] The achievement of this high confinement mode has been attributed to impurity recycling effects related to the divertor.[23,24] An internal mode, known as the fishbone instability, has been shown to limit the plasma beta.[25] These recently observed effects and the role played by impurities in them are not fully understood. The achievement of low safety factor q operation in Tokapole II may also be related to the divertor configuration and profile effects.[26]

Control of impurities is a major concern of all tokamaks. Material selection includes consideration of cleanliness, vacuum and mechanical properties, atomic number, and ability to withstand particle and thermal loads. For reactors the criteria will be even more stringent, as described in Reference 27. Conditioning procedures for walls and limiters, such as pulsed discharge cleaning,[28] titanium coating,[29], and glow discharge cleaning,[30] are used to eliminate the adsorbed water and carbon compounds as much as possible. Efforts to control the flow of impurities with divertors are being tested on several large tokamaks, particularly ASDEX, PDX, Doublet III, and DITE.[31] New limiter designs such as pumped limiters are also being investigated.[32] Greater understanding of the role of impurities at the edge and in the central current channel is

necessary for control of the minimal levels of impurities that will have to be tolerated in a reactor.

B. Outline of the Results of this Research

This thesis describes a series of experiments designed to characterize the impurity release mechanisms in Tokapole II. For one case, the early generation of the light impurities, a definite identification of the mechanism, ion-induced desorption, has been made. For this case a detailed study of the parameter behavior of the release mechanism in impurity doping and isotopic exchange experiments has been compared with a model of the time-dependent impurity influx. Additionally the edge parameters have been measured under a variety of start-up conditions, in conjunction with other start-up work performed on Tokapole II.[33] With a comparison to light impurity behavior during start-up, the identification of metal production mechanisms can be made tentatively as well. Secondary goals of the research have been to identify the impurity release mechanisms during the steady-state phase and to study the effects of impurities on the plasma behavior. The use of spectroscopic diagnostics to study the impurity behavior has followed closely the initial work on Tokapole II of R.J. Groebner.[34]

The major result of this research is the experimental description of the ion-induced desorption mechanism during start-up. A description of Tokapole II, the tokamak used for these experiments, with the present settings used for a standard

discharge, the plasma parameters for this typical case, and a summary of the impurity characteristics are presented in Chapter 2. The experimental data from the doping and isotopic exchange experiments are given in Chapter 3. This chapter shows the mass-dependent effects of dopant and working gases on light impurity concentrations. With the use of a time-dependent coronal equilibrium model to unfold the spectroscopic information, and the cross sections for desorption from the literature, one can model the influx of light impurities during start-up, as described in Chapter 4.

A description of experiments on the metal impurity production during start-up is given in Chapter 5. The information obtained about the initial impurity evolution then suggests interpretations of the start-up process. A discussion of this process and a presentation of data taken to examine the interrelated effects of the wall condition, the start-up procedure, and the plasma parameters in the edge follow in Chapter 6. Profile data are shown for some impurity states. Chapter 7 includes a summary of the research results, conclusions, and suggestions for further work.

REFERENCES

[1]G.M. McCracken and P.E. Stott, Nucl. Fusion 19 (1979) 889. This reference is an excellent review article on "Plasma-Surface Interactions in Tokamaks."

[2]G.M. McCracken, J. Nucl. Mater. 93/94 (1980) 3.

[3]H. Ohtsuka, M. Maeno, N. Suzuki, S. Konoshima, S. Yamamoto, N. Ogiwara, Nucl. Fusion 22 (1982) 823.

[4]R.J. Taylor and Lena Oren, Phys. Rev. Lett. 42 (1979) 446.

[5]W. Bauer, J. Nucl. Mater. 76/77 (1978) 3.

[6]R.J. Fonck, M. Finkenthal, R.J. Goldston, D.L. Herndon, R.A. Hulse, R. Kaita, and D.D. Meyerhofer, Phys. Rev. Lett. 49 (1982) 737.

[7]G.M. McCracken, S. Cohen, H.F. Dylla, C.W. Magee, S.T. Picraux, S.M. Rossnagel and W.R. Wampler, in: Proc. 9th European Conf. on Controlled Fusion and Plasma Physics, Oxford, 1979, Vol. 1 (1979) 89.

[8]G. Staudenmaier, P. Staib, R. Behrisch and Equipe TFR, Nucl. Fusion 20 (1980) 96.

[9]N. Suzuki, N. Fujisawa, S. Konoshima, M. Maeno, M. Shimada, T. Yamamoto, S. Kasai and K. Uehara, in: Proc. 9th European Conf. on Controlled Fusion and Plasma Physics, Oxford, 1979, Vol. 1 (1979) 90.

[10]S. Suckewer and R.J. Hawryluk, Phys. Rev. Lett. 40 (1978) 1649.

[11]S.A. Cohen, H.F. Dylla, S.M. Rossnagel, S.T. Picraux and C.W. Magee, J. Nucl. Mater. 76/77 (1978) 459.

[12]H. Ohtsuka, Nucl. Fusion 22 (1982) 827.

[13]G.M. McCracken, S.J. Fielding, and H. Ohtsuka, J. Nucl. Mater. 111/112 (1982) 396.

[14]S.J. Fielding and A.D. Sanderson, J. Nucl. Mater. 93/94 (1980) 220.

[15]See, for example, Sections 2 and 3 on Plasma Edge Experiments in: J. Nucl. Mater. 111/112 (1982).

[16]See the recent review article by D.E. Post, D.B. Heifetz, and M. Petravic, J. Nucl. Mater. 111/112 (1982) 383.

[17]R.A. Gross, B. Jensen, J.K. Tien, and N. Panayotou, in Plasma-Wall Interactions (Proc. Int. Symp. Julich, 1976) Pergamon Press, New York (1977) 659.

[18]J.K. Tien, N.F. Panayotou, R.D. Stevenson, and R.A. Gross, J. Nucl. Mater. 76/77 (1978) 481.

[19]D.M. Meade, Nucl. Fusion 14 (1974) 289.

[20]R.J. Hawryluk and J.A. Schmidt, Nucl. Fusion 16 (1976) 775.

[21]R.C. Isler, B.A.P.S. 28 (1983) 1053.

[22]F. Wagner et al., Phys. Rev. Letts. 49 (1982) 1408.

[23]ASDEX team, B.A.P.S. 28 (1983) 1052.

[24]R.J. Fonck, B.A.P.S. 28 (1983) 1052.

[25]K. McGuire et al., Phys. Rev. Letts. 50 (1983) 891.

[26]T.H. Osborne and N.S. Brickhouse, University of Wisconsin Plasma Studies PLP 908 (1983).

[27]H. Vernickel, J. Nucl. Mater. 111/112 (1982) 531.

[28]L. Oren and R.J. Taylor, Nucl. Fusion 17 (1977) 1143.

[29]P.E. Stott, C.C. Daughney, and R.A. Ellis, Nucl. Fusion 15 (1975) 431.

[30]H.F. Dylla, S.A. Cohen, S.M. Rossnagel, G.M. McCracken, Ph. Staib, presented at 26th National Symposium of the American Vacuum Society (1979).

[31]M. Keilhacker and K. Lackner, J. Nucl. Mater. 111/112 (1982) 370.

[32]P. Mioduszewski, J. Nucl. Mater. 111/112 (1982) 253.

[33]D.J. Holly, S.C. Prager, D.A. Shepard, and J.C. Sprott, Nucl. Fusion 21 (1981) 1483.

[34]R.J. Groebner, Ph.D. Thesis, University of Wisconsin (1979).

CHAPTER 2

TOKAPOLE II OPERATING CONDITIONS

A. Tokapole II - The Machine

Tokapole II has been operated as a four-node poloidal divertor tokamak for the experiments described in this thesis. These experiments have been performed over the period from March 1979 to April 1983. The Tokapole II device has been described in more detail elsewhere.[1,2] The aluminum vacuum vessel is a torus with a 44 cm square cross section and a 50 cm major radius (Figure 2-1). Four internal rings of 5 cm minor diameter, supported inside the tank (Figure 2-2), are used to generate the divertor configuration. The solid rings are made of a high conductivity chromium-copper alloy; the support rods are made of a beryllium-copper alloy.

The vacuum poloidal field (Figure 2-3) is created by currents in the rings, driven inductively by a 7.2 mF, 5 kV (90 kJ) capacitor bank through an iron core transformer. The 40:1 turns ratio on the transformer gives a sinusoidal field shape in time which has a half period of 5.6 ms. The poloidal field is generally crowbarred actively, by adding a 450 volt, 0.96 F (97 kJ) capacitor bank. In the spring of 1981, a damping resistance was added to the primary circuit for the standard operating procedure in order to shorten the initial voltage spike. Figure 2-4a shows the resulting poloidal gap

Figure 2-1. Tokapole II.

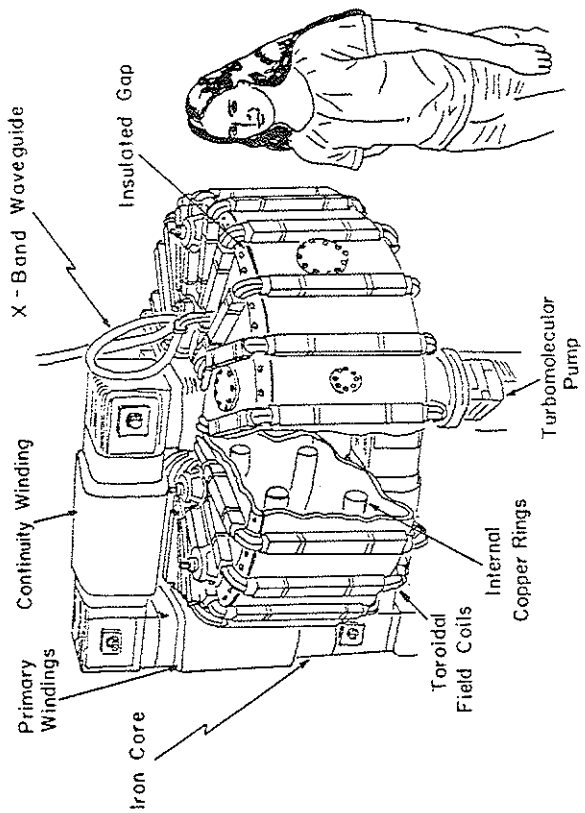

Figure 2-1

Figure 2-2. Cross section of vacuum vessel showing internal rings.

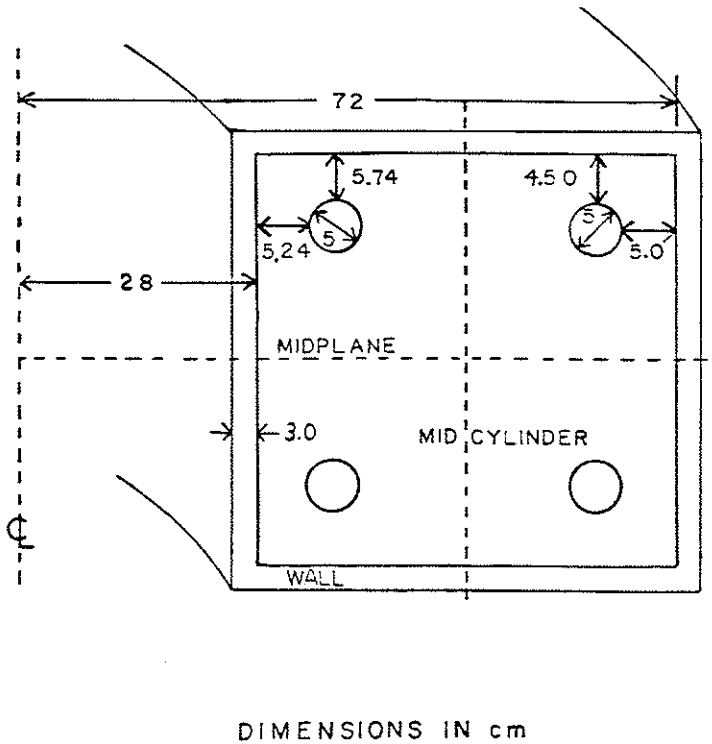

Figure 2-2

Figure 2-3. Vacuum poloidal magnetic field flux plot. The major radius R is measured from the center of the torus. The vertical scale is measured from the center of the vacuum vessel. Dimension are in m.

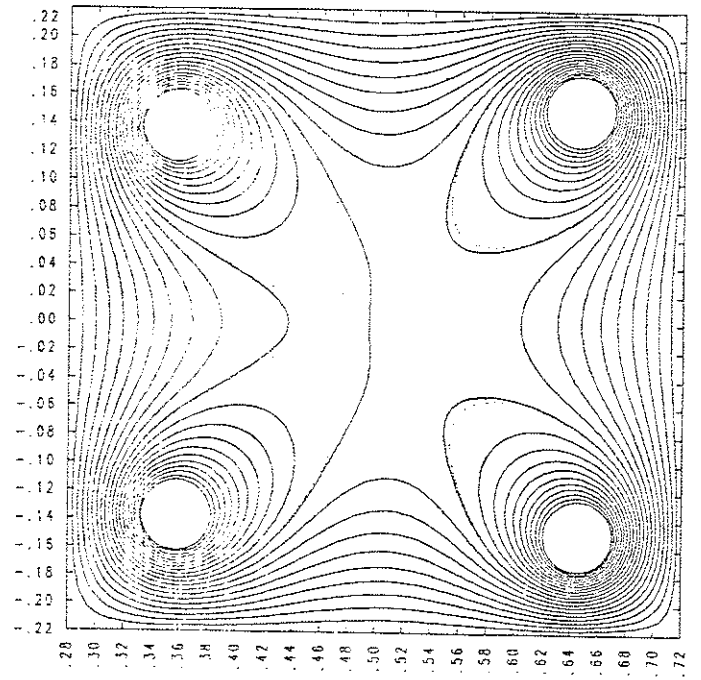

Figure 2-3

Figure 2-4a. Timing of poloidal gap voltage. Discharges prior to February 1981 were made without damping resistance. Since 1981 standard discharges have used damping resistance.

Figure 2-4b. Timing of toroidal magnetic field.

Figure 2-4

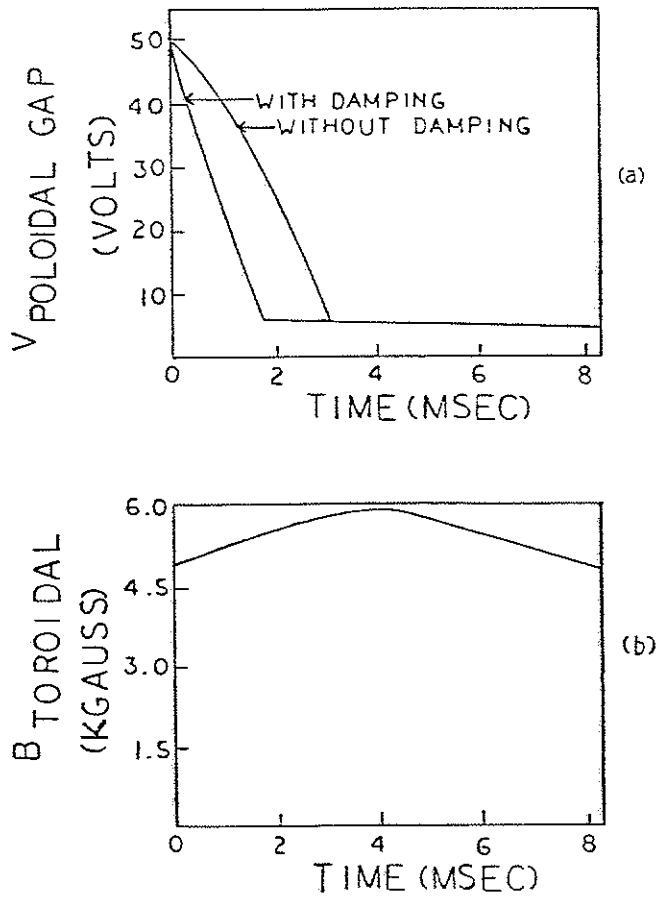

voltages produced. The total flux available in the core is 0.15 webers. Since image currents of the ring currents flow in the 3 cm thick conducting walls, the magnetic symmetry should be improved over machines with non-conducting walls. At the poloidal gap, continuity windings return the wall currents around the transformer core. The vertical positions of the rings may be varied $\pm$ 5.0 mm to change the position of the vacuum field null. The existence of the null allows for some plasma current to start up away from the walls. The equilibrium of the plasma is quite sensitive to the position of the rings as well.

The toroidal field, $B_{toroidal}$ (Figure 2-4b), is created by external windings driven by 52 mF, 5 kV (650 kJ) capacitor bank. The half period is about 10 msec. The image currents in the conducting walls produce uniform toroidal field in the machine despite the widely spaced field windings. The field is passively crowbarred near peak field, which has been gradually increased from about 4 kG to 6 kG as the standard operating field on axis.

During the course of these experiments, many vacuum pumping and wall conditioning systems have been used. In 1979, both a turbomolecular pump and a helium cryogenic pump were used to maintain base pressures in the low 10^{-7} to high 10^{-8} torr range. The walls were baked to 75°C overnight and cooled to <50°C during the day. The wall conditioning procedure used overnight was a pulsed discharge cleaning technique, demonstrated by Taylor to be effective in removing surface contaminants.[3] Since 1980 the cryopump

has been abandoned, originally for long-term maintenance, and also now for additional port access for diagnostics. The bake/cool cycling has not been operational for the last few years due to known air leaks opening in the triple joint (where the toroidal and poloidal gaps meet) during temperature cycling. The machine is currently held at about 50°C. In early 1980, overnight pulsing was replaced by glow discharge cleaning in hydrogen.[4] For Tokapole II the procedure consists of biasing the rings positive with respect to the wall with a high voltage (roughly 300 to 400 V) and filling the tank with about 30 mtorr of extremely pure hydrogen. At the present settings, the wall draws a positive current of about 120 mA whereas the rings draw about 60 mA of negative current. Many configurations have been used in the past, including a long run with higher current to the rings, which may have resulted in copper sputtering. Glow discharge cleaning had two immediate advantages, due to its more intense conditioning of the vacuum surfaces. A marked improvement in the discharge parameters was observed in general, and the deleterious effects of air venting the machine were minimized. With an overnight glow, the machine could produce reasonable discharges the day after an air venting, whereas pulsed discharge cleaning had taken about a week to achieve normal operation. Currently there is concern that continued glow discharge cleaning is having some bad effects as well, primarily because of the sputtering of copper from the rings to all surfaces. A new pulsed discharge cleaning system and a titanium coating scheme (which would also improve the base

pressure) are being designed, and should be operational soon. Initial experiments have indicated that a combination of the three procedures, with minimal glow discharge cleaning to avoid sputtering copper, should produce reasonable wall conditions.

The chamber is filled to 3×10^{-4} torr with the working gas, usually hydrogen, prior to the field pulses. A fast piezoelectric puff valve is used. Additional gas may be puffed during the discharge, either in stages with fixed amplitudes, or with a feedback circuit which has a time response of about 1 msec and is controlled by the line-averaged ion saturation diagnostic in the edge region. Microwave pre-ionization at the electron cyclotron frequency (ECRH) can be used to aid the start-up. Three types of sources are available: a continuous 100 W S-band (2.45 GHz), a pulsed 10 kW X-band (9 GHz), and two pulsed 5 kW K-band (16.5 GHz), with pulse lengths of 500 μsec. An applied d.c. vertical field can also be used to produce 10 Gauss on axis. This field seems to push the magnetic axis, which usually sits out a few cm, back towards the center, particularly for discharges with low plasma current.

Scrape-off plates may be inserted up to the separatrix (Figure 2-5) from all four sides at one toroidal azimuth; however, for the research presented in this thesis, the Tokapole has been operated without scrape-off plates. Roughly one-third of the plasma current flows in the common flux region (the region enclosing all four rings) during start-up. A study of edge parameters during the steady-state has been made recently[5] for the two cases; the impurity

Figure 2-5. Central current channel separated from common flux or scrape-off region by separatrix (dashed line). Four scrape-off plates, or limiters, may be inserted to the separatrix. For the limiter cases discussed here only three scrape-off plates were used, with their extension into the tank approximately as shown.

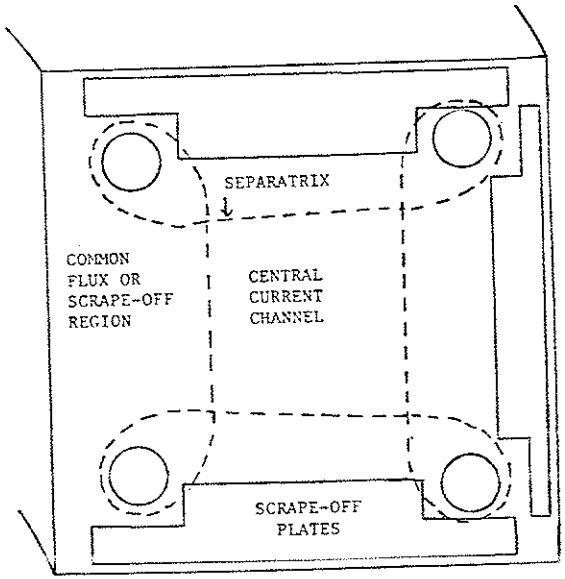

THE TOKAPOLE II DIVERTOR CONFIGURATION

Figure 2-5

profiles observed spectroscopically are consistent with the measurements.

B. Plasma Characteristics

In this section the basic plasma parameters as measured by various diagnostics are reviewed. Since the plasma-wall interaction experiments have been conducted over a wide range of discharge conditions, the data presented in this section are intended to be representative of the plasma parameters. The impurity production mechanisms have been essentially the same throughout the variations of magnetic fields, base vacuum pressures, cleaning techniques, and other parameters.

In the spring of 1979 Tokapole II had been in operation for about one year, during which time reasonable operating parameters and cleanliness had been achieved, although the discharge duration was only about 4 msec. Data from these short-lived discharges can be found in References 2 and 6. Since then the discharge length has been increased to 12 msec (15 msec maximum achieved) by conditioning the vacuum vessel walls, increasing the toroidal field, and using late gas puffing. The peak T_e and $\bar{n}_e$ have not been significantly improved; however, the major accomplishment has been the achievement of several msec of steady-state operation. The energy confinement time is now about 0.5 msec, roughly in accord with tokamak scaling.[7]

A theoretical poloidal magnetic field flux plot[8] is shown in Figure 2-6 for standard toroidal field and current. Both square and dee-shaped equilibria have been measured with magnetic probes.[9] The discharge can be divided into two time phases: the start-up phase, roughly the first 1.5 to 2.5 msec, during which peak current and density occur and the plasma heats up to its peak temperature, and the plateau or steady-state phase, during which the parameters are essentially constant until the plasma runs out of volt-sec. Figures 2-7 and 2-8 illustrate the plasma behavior for two different poloidal gap voltages, with all other parameters fixed.

The plasma current is difficult to determine accurately since it is only about 20% of the current in the rings. The routine plasma current monitor estimates the total plasma current by measuring the poloidal gap voltage and the current in the transformer primary, and modeling the plasma as an element in the ohmic heating transformer secondary. This monitor is accurate to about 25% during steady-state, as verified with a large Rogowski coil,[2,10,11] but overestimates the start-up current near the walls by as much as a factor of two. The plasma current monitor gives the peak I_p between 30 and 50 kA, with 10 to 25 kA during the steady-state phase. (Figures 2-7a and 2-8a).

The initial gas concentration, measured with a Bayard-Alpert Fast Ionization Gauge, is equivalent to 1×10^{13} cm^{-3} of fully ionized H_2 gas. The peak of the line-average electron density, $\bar{n}_e$ (Figures 2-7b and 2-8b), measured with a 70 GHz microwave

Figure 2-6. Poloidal magnetic flux plot calculated with an MHD equilibrium code. This case is representative of the higher I_{plasma}, $B_{toroidal}$ plasmas. The dotted lines are the separatrices.

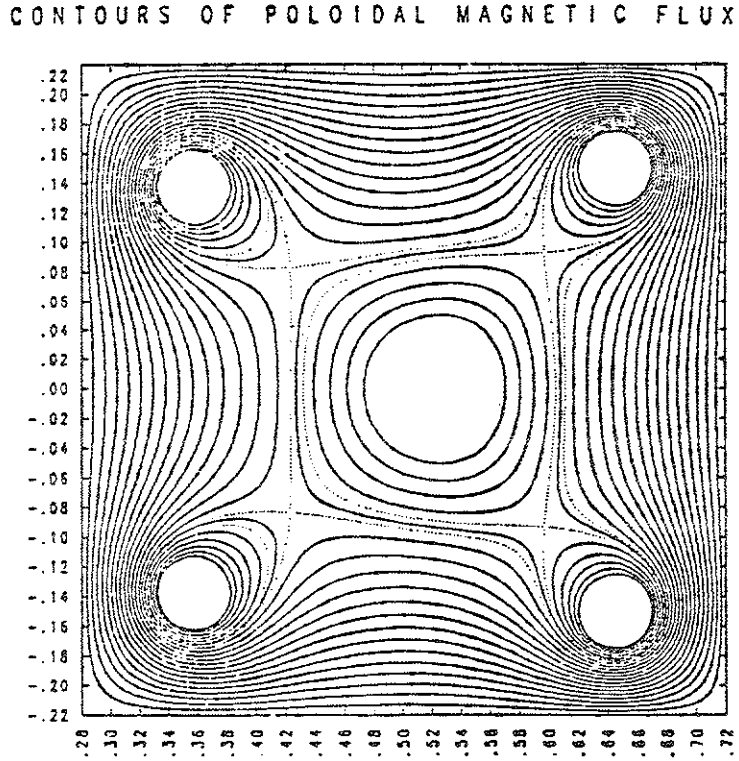

Figure 2-6

Figure 2-7a. Plasma current versus time for a standard discharge with higher peak current, using $V_{poloidal\ gap}$ and $B_{toroidal}$ of Figure 2-4. This case is represented by the theoretical flux plot of Figure 2-6. The measurements shown in this Figure are for the same shot.

Figure 2-7b. Line-average electron density versus time.

Figure 2-7c. Central chord SXR signal versus time, showing the time of the T_e peak.

Figure 2-7d. Ion saturation current density measured with a line-average Langmuir probe in the edge. This signal represents the edge density and is used for the late gas puffing feedback circuit.

Figure 2-7a and 2-7b

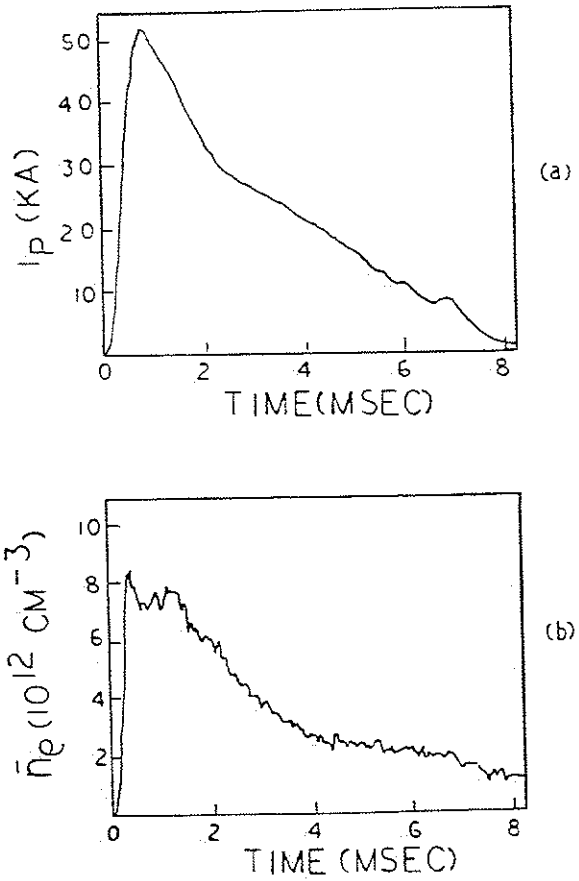

Figure 2-7c and 2-7d

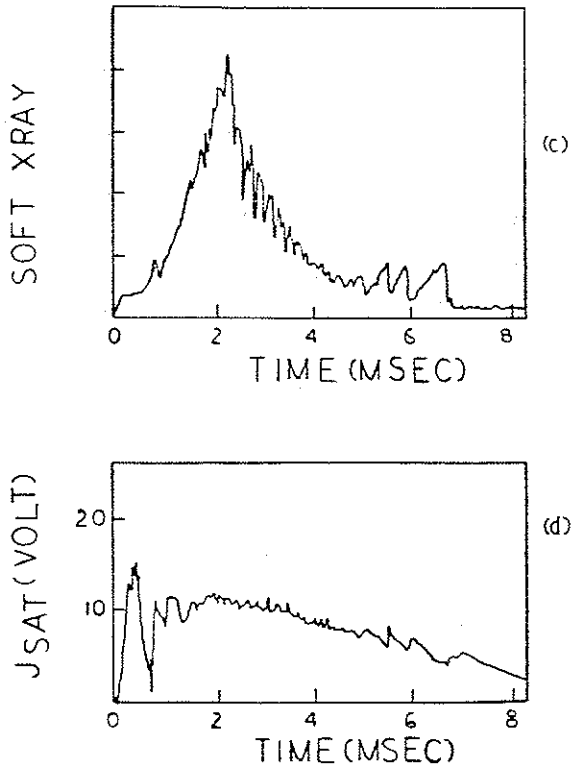

Figure 2-8a. Plasma current versus time for a lower $V_{poloidal\ gap}$ than in Figure 2-7. All other settings are the same as for Figure 2-7. All measurements shown in this Figure are for the same discharge.

Figure 2-8b. Line-average electron density versus time.

Figure 2-8c. Central chord SXR signal versus time.

Figure 2-8d. Edge ion saturation current density versus time.

Figure 2-8a and 2-8b

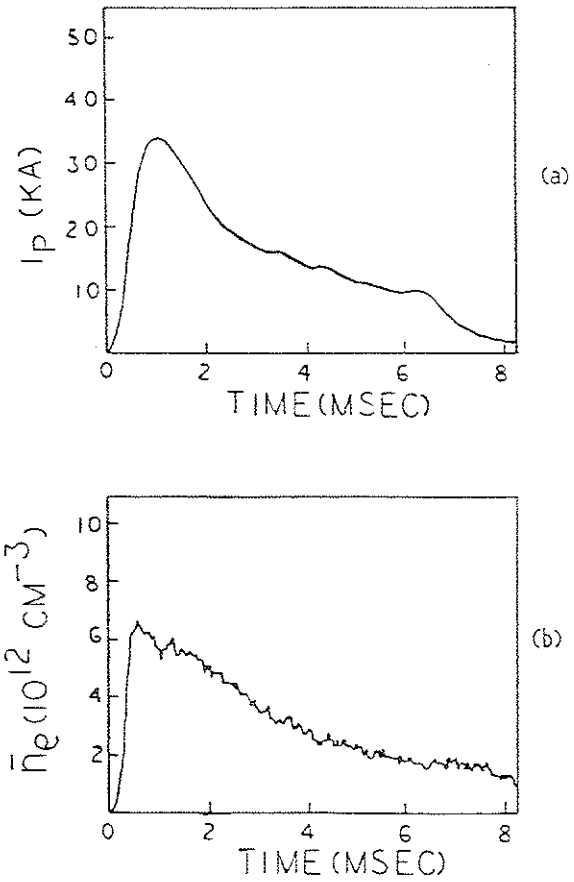

Figure 2-8c and 2-8d

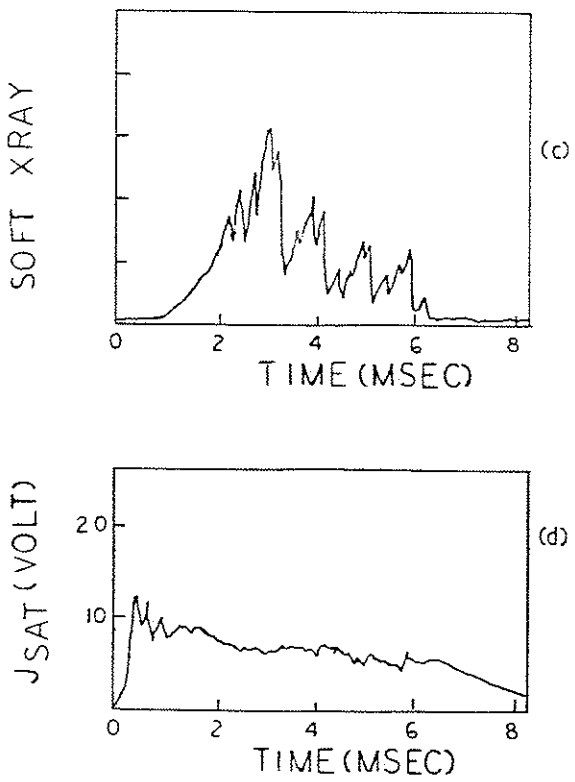

interferometer viewing the midcylinder from the top of the machine, is 6 to 8 x 10^{12} cm^{-3} at 0.3 to 0.4 msec, dropping to a steady-state value of 2 to 3 x 10^{12} cm^{-3}. The peak of the electron temperature, T_e, has been estimated to be about 100 eV by two techniques. A spectroscopic measurement of the oxygen series line radiation in the Vacuum Ultraviolet (VUV) with an absolutely calibrated 1-m Seya VUV monochromator, in combination with a time-dependent coronal model, gives the time evolution of T_e during the start-up phase.[12] The conductivity temperature measured by current density and toroidal electric field probes has given rough agreement for Z_{eff}, the effective ionic charge of the plasma, of 2.5 to 3.0. The electron temperature peaks between 2 and 3 msec, as illustrated by the central chord soft xray (SXR) emission (Figures 2-7c and 2-8c). The SXR detectors are surface barrier diodes with polypropylene filters which limit the transmission to the energy range 60 eV to 300 eV. The detectors have approximately an exponential dependence on T_e for Tokapole energy ranges.[13]

A routine diagnostic for edge densities and temperatures is the three-tipped line-average Langmuir probe located on the vacuum separatrix between the lower ring and the outer wall. The edge density is represented by the probe measurement of ion saturation current density, J_{SAT}, in the common flux region (Figures 2-7d and 2-8d).

C. Description of Impurities

Spectroscopic measurements of impurity radiation have been made using an absolutely calibrated 1-m Seya VUV monochromator which views a chord through the center of the plasma, a VUV survey system consisting of a 1/2-m Seya spectrometer with a microchannel plate in its exit plane, capable of time-gated operation in the 400-1300 Å region of the VUV, and two 1/2-m Jarrell-Ash visible monochromators with tilting capabilities. A tiltable integrated VUV detector and an array of SXR detectors provide spatial information on the impurity radiation as well as total power radiated in these regions. These diagnostics are described in more detail elsewhere.[2,12,14] For routine monitoring of impurity levels a set of four photomultipliers is mounted on the top of the machine with filters for visible radiation. A grazing incidence monochromator for observation of the wavelength region between the VUV and the SXR regions is currently being tested.

During the first year of operation the Tokapole discharge parameters improved significantly, primarily due to a decrease in the impurity levels with discharge cleaning. Since then, and for the duration of this research, the concentration of impurities during the start-up has remained essentially the same. The line radiation for these standard discharges is less than 25% of the ohmic input power and thus cannot be the dominant energy loss mechanism. The low-Z impurity concentrations have been estimated by

an impurity doping method (described in Chapter 3). The major low-Z impurities are oxygen (2×10^{11} cm^{-3}), carbon (5×10^{10} cm^{-3}), and nitrogen (3×10^{10} cm^{-3}). For the metal impurity concentrations, primarily aluminum and copper, an estimate has been made by comparing the low-Z impurity contribution to the integrated VUV radiation. The metal impurities must then account for about 40% of the VUV radiation.[12] Major impurity lines, measured photographically with the VUV survey spectrometer and output to the densitometer in the U.W. Biochemistry Department, are shown in Figure 2-9 for the start-up phase.

The impurity ion radiation observed on tokamaks is characterized by two distinct behaviors: an ionization peak during the start-up phase, when ohmic heating of the volume causes the burnout from lower to higher ionization states, and a plateau level, when each ionic state peaks its profile at the location where T_e is roughly one-third of its ionization potential.[15] Groebner presents data from the spring of 1979 with distinct ionization peaks, but with plateau levels similar in magnitude to the peaks and often with second peaks as well. (See Reference 2, p.129.) Although the start-up impurity levels have remained similar, a large improvement in the plateau behavior has occurred. The plateau levels are now low and extremely constant in time. The time-dependent signals of several bright impurity lines are shown in Figure 2-10. The improvement can be attributed both to a decrease of local sources from unconditioned wall or ring areas and to a decrease in the

Figure 2-9. A sequence of pictures obtained for consecutive discharges with the VUV survey instrument microchannel plate. The gate is on in each case for 0.4 msec. These pictures illustrate the evolution of the VUV spectrum with time from bottom to top.

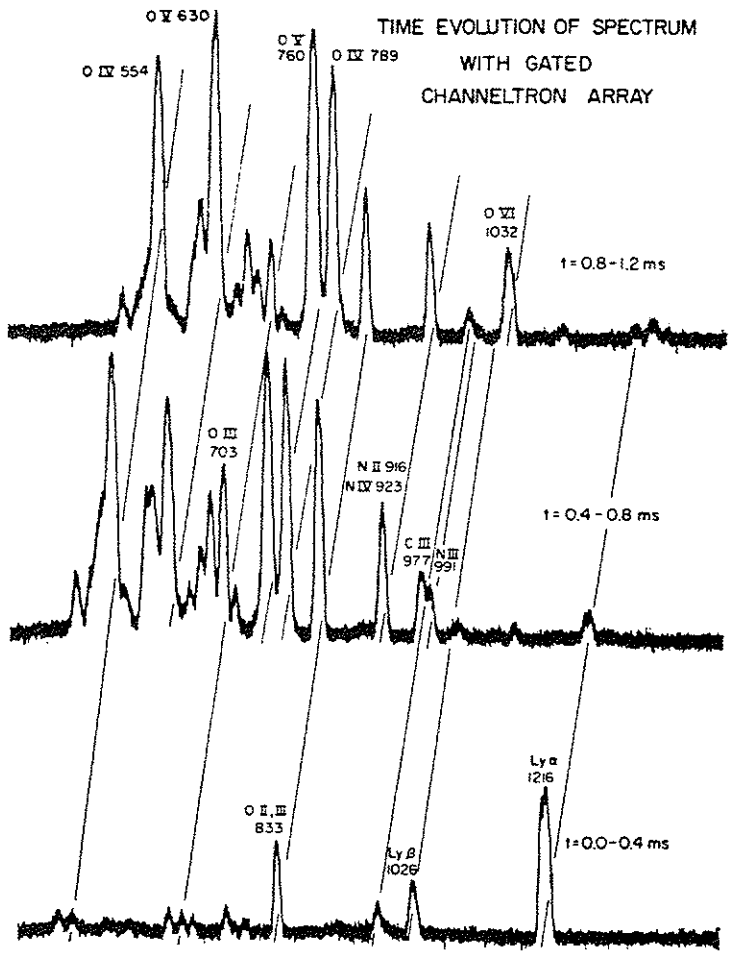

Figure 2-9

Figure 2-10a. Impurity line radiation versus time for a standard discharge. (The end of the discharge at 12 msec is not shown.) This data was taken with the 1-m Seya VUV monochromator. Several important impurity lines are shown.

Figure 2-10b. Impurity line radiation versus time for the same discharge of Figure 2-10a. This data was taken with the routine impurity monitor with filtered photomultipliers.

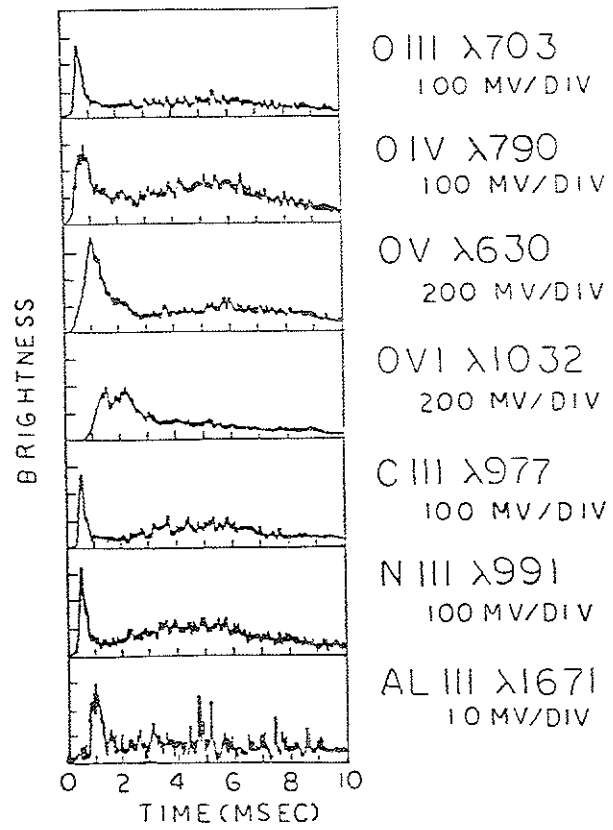

Figure 2-10a

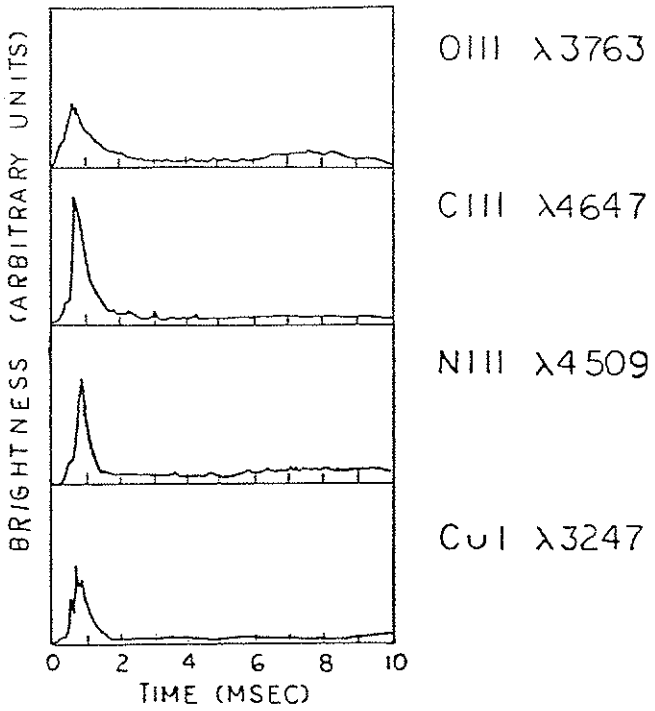

Figure 2-10b

impurity influx. The decrease in influx may imply an improvement in particle confinement (consistent with a measured improvement in the energy confinement time), which may be effectively an improvement in the plasma's ability to shield its hot central core from the plasma boundary region, where rapid recycling must certainly occur.

REFERENCES

[1]J.C. Sprott, University of Wisconsin Plasma Studies PLP 744 (1978).

[2]R.J. Groebner, Ph.D. Thesis, University of Wisconsin (1979).

[3]L. Oren and R.J. Taylor, Nucl. Fusion 17 (1977) 1143.

[4]H.F. Dylla, S.A. Cohen, S.M. Rossnagel, G.M. McCracken, and Ph. Staib, "Glow Discharge Conditioning of the PDX Vacuum Vessel," presented at the 26th National Symposium of the American Vacuum Society, New York (1979).

[5]T.D. Rempel and G.A. Emmert, University of Wisconsin Plasma Studies PLP 894 (1983).

[6]A.P. Biddle, R.N. Dexter, R.J. Groebner, D.J. Holly, B. Lipschultz, M.W. Phillips, S.C. Prager, and J.C. Sprott, Nucl. Fusion 19 (1979) 1509.

[7]J.C. Sprott, University of Wisconsin Plasma Studies PLP 877 (1982).

[8]M.W. Phillips, University of Wisconsin Plasma Studies PLP 765 (1978).

[9]B. Lipschultz, S.C. Prager, T.H. Osborne, J.C. Sprott, and M. Phillips, Phys. Rev. Lett. 43 (1979) 36.

[10]J.C. Sprott, University of Wisconsin Plasma Studies PLP 712 (1977).

[11]S.C. Prager, J.C. Sprott, T.H. Osborne, and K. Miller, University of Wisconsin Plasma Studies PLP 756 (1978).

[12]R.J. Groebner and R.N. Dexter, Plasma Physics 23 (1981) 693.

[13]R.J. Groebner and R.N. Dexter, University of Wisconsin Plasma Studies PLP 770 (1978).

[14]R.N. Dexter and R.J. Groebner, University of Wisconsin Plasma Studies PLP 768 (1978).

[15]T.F.R. Group, Plasma Physics 20 (1978) 207.

CHAPTER 3

ION-INDUCED DESORPTION DURING START-UP -- EXPERIMENTS

A. Impurity Doping Experiments

This section describes the experimental procedure and results for the doping experiments. The major result of these doping experiments is that the generation of the light impurities, oxygen (O), carbon (C), and nitrogen (N), increases with the concentration of any doped gas such that this increase per dopant atom is proportional to the dopant mass. This result implicates ion-induced desorption as the major process for introducing light impurities into Tokapole II plasmas. Many dopant gases (D_2, He, CH_4, N_2, O_2, Ne, Ar, Kr, and Xe) have been used for this series of experiments, during which impurity line radiation signals for O, C, and N have been observed.

The dopant gas is added to a fixed concentration of the working gas, usually hydrogen. The hydrogen puff valve is opened 16.7 msec before the discharge starts in order to allow time for uniform filling of the machine. For higher mass gases the dopant gas puff valve must be opened even earlier, with a typical delay of 25 msec between this valve opening and the poloidal field triggering. A maximum delay of 40 msec has been used for the series including Xe, the heaviest dopant gas used. The timing is usually set so that the

fast ionization gauge, used to measure the gas concentrations, reads the peak of the dopant gas signal prior to the hydrogen puff. The calibration of the gauge for different gases uses the coefficients of Lewin[1] and Dushman.[2] The line radiation signals for the exotic gas dopants are proportional to the concentration measured by the ionization gauge.

Doping with any gas causes radiation signals from all light impurities to increase, as shown in Figure 3-1. The largest increase is during the impurity ionization phase, with a small increase, if any, during the plasma current plateau. Figure 3-2 illustrates the early time-dependence of the effects of 2% Ar concentration on the OIII λ703 line radiation signal. As the dopant concentrations increase the line radiation signals also increase. For dopant levels up to those levels needed to double the spectral line intensities of the ionization peak (dopant concentrations less than 10% of atomic H concentrations) the increase is linear, except for self-desorption, although higher dopant levels lead to nonlinearity (see Section C). The increase in the ionization peaks with added hydrogen gas is shown in Figure 3-3. Typical data for an impurity doping series are shown in Figure 3-4.

The data of Figure 3-4 suggest that the impurity levels depend not only on the dopant concentration, but also quite strongly on the dopant mass. In order to assess the error in assuming that changes in line radiation signals reflect changes in the impurity ion concentrations in the plasma, the relative changes in n_e and T_e over

Figure 3-1. Densitometer trace of VUV spectrum with no doping (bold line) and for Ar doping (light line), using the time-gated spectrometer (gated on between 0.5 and 1.0 msec). This Figure illustrates the increase of light impurities with doping. The nonlinearity of the photographic emulsion prevents this technique from being used for quantitative measurements; instead, monochromators with photomultipliers are used.

Figure 3-1

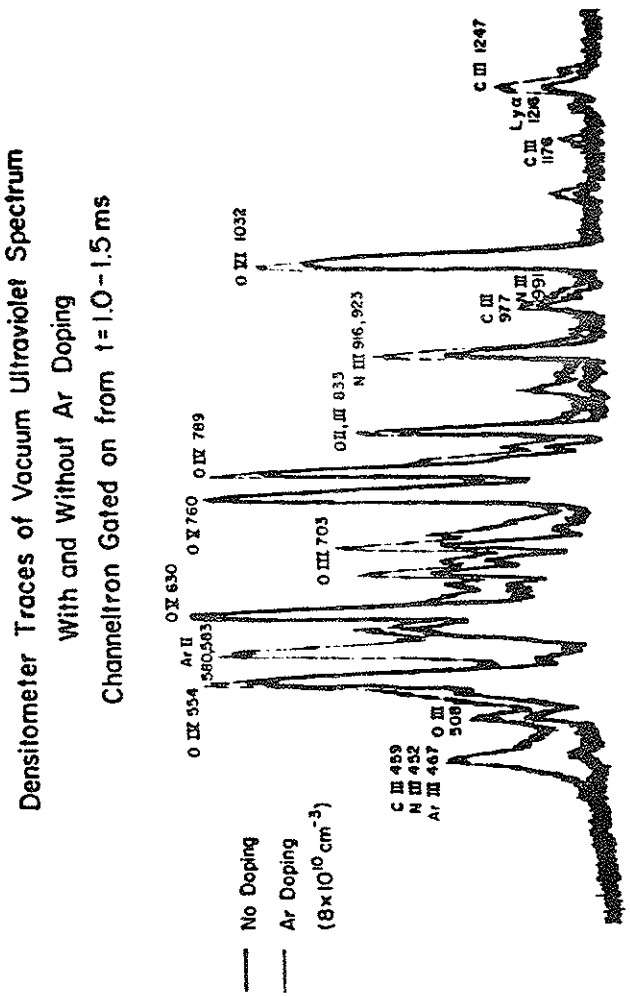

Figure 3-2. OIII λ703 signal as a function of time during start-up for cases with and without doping.

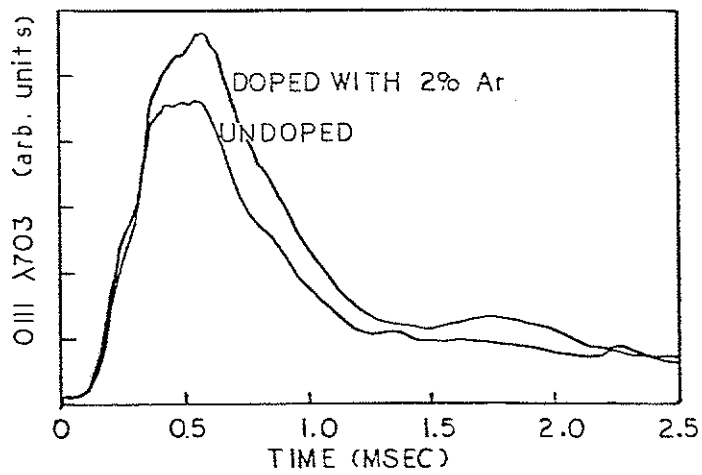

Figure 3-2

Figure 3-3. OIII λ703 and NIII λ4511 versus added H, for a puffed H concentration of about 9.8×10^{12} atoms/cm^3 and a peak interferometer density of 4.2×10^{12}/cm^3.

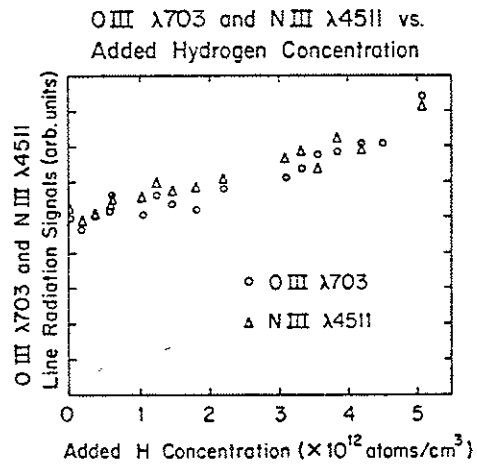

Figure 3-3

Figure 3-4. OIII λ703 ionization peak as a function of dopant concentration for various dopant gases. For Ar, the set of data points is shown. The error bars on the point on the He plot show the typical shot to shot variation for a data point.

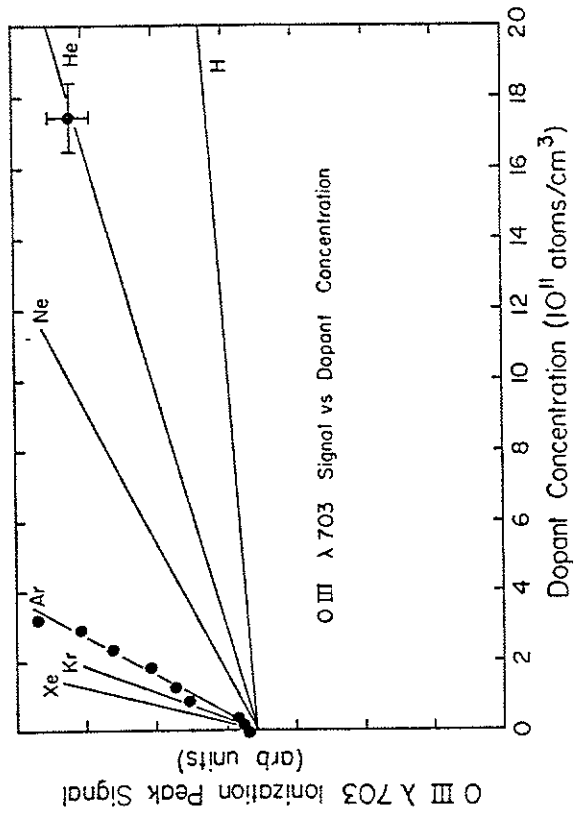

Figure 3-4

a doping run must be determined. The impurity line radiation signals are proportional to $n_e n_i Q(T_e)$, where Q depends on the ionic state. From microwave interferometer and probe measurements of n_e during doping, the change in n_e accounts for less than 20% of the increase in the impurity radiation. Figure 3-5 shows that OIII increases significantly faster than $\bar{n}_e$ with N doping.

With the VUV monochromator and SXR detectors an estimate of the change in T_e caused by doping can be made. Temperature profile modifications and changes in the rate of increase of T_e during current channel buildup, as well as decreases in the peak T_e, may all contribute to changes in impurity line radiation with doping. Two methods used to estimate the volume-averaged $T_e(t)$ are: a separation of the strong T_e-dependence of SXR signals from the weaker dependence on n_e and n_i by comparison with the integrated VUV and interferometer, and a coronal model of the oxygen series, OII through OVI[3] (see Chapter 4). The coronal model fits $T_e(t)$ for the undoped plasma to the time evolution of the oxygen ionic states. T_e increases up to about 20 eV by about 200 μsec, remains flat until OIII peaks between 600 and 800 μsec, then rises sharply to 130 eV by the SXR peak time at 2.5 msec, as shown in Figure 3-6. For the maximum dopant concentration used (which doubles OIII), the coronal model fit for T_e shows little effect for the 20 eV phase, but shows that T_e can peak up to 350 μsec later at 100 eV. The magnitude of the SXR changes agrees well with the measured $\bar{n}_e$ change and the T_e change found from the model. The relative increase in the SXR

Figure 3-5. A comparison of line radiation signal and electron density as measured with a microwave interferometer. This Figure shows that the increase in n_e is not a significant contribution to line radiation signal increases. (OIII signal is porportional to $n_e n_i Q(T_e)$.) This plot includes high dopant levels.

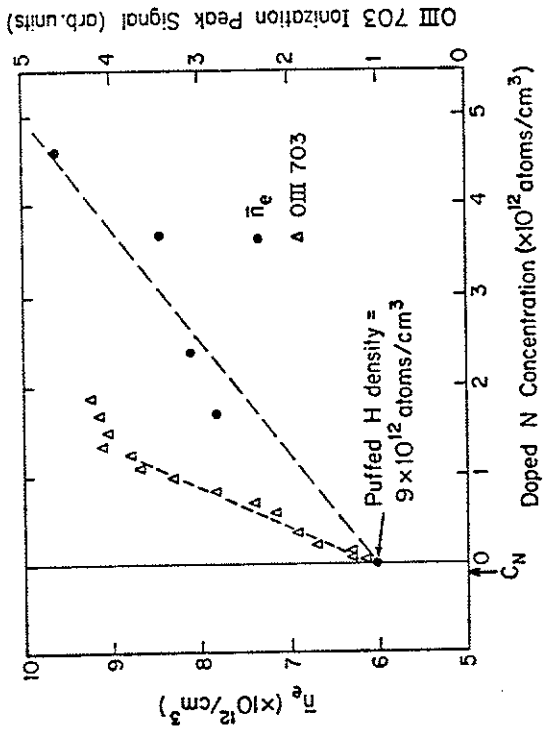

Figure 3-5

Figure 3-6. Simulations for $T_e(t)$ based on coronal model of oxygen series data for cases with and without doping. (See Chapter 4.)

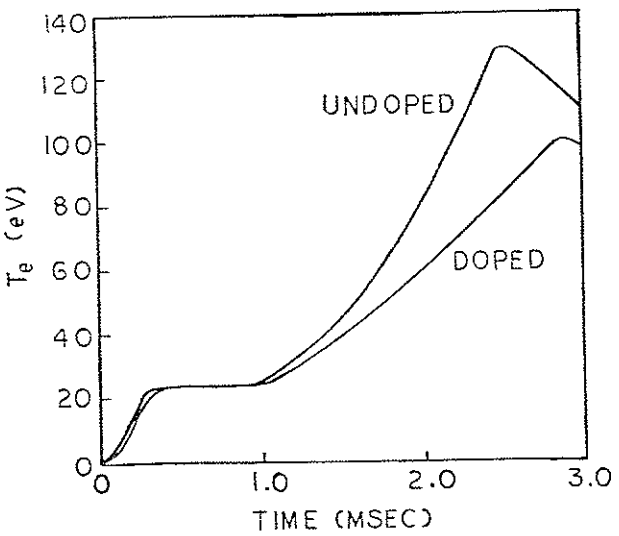

Figure 3-6

signal for early times is less than the relative increase in VUV radiation. Both signals are proportional to the line-averaged product $n_e n_i$ but SXR is a strong function of T_e, whereas VUV has only a weak dependence on T_e.

For small changes in n_e and T_e, then, a linear increase in impurity line radiation implies a proportional increase in the impurity concentration. The error in this proportionality factor is estimated by comparing the increase in various oxygen series lines during doping. The increases per dopant atom of OII λ797, OIII λ703, OIV λ789, and OV λ630 are within a factor of two of each other, as shown in Figures 3-7 and 3-8. Different dopants tend to produce changes in the oxygen radiation in the same way. Most of the mass-dependence studies have used the lower ionization state OIII (also NIII, CIII) for several reasons. The function $Q(T_e)$ for OIII λ703 is only weakly dependent on T_e. The peak time of OIII varies the least with doping, unlike OVI, which peaks 300 to 400 μsec later for modest doping. The time variation of the OVI λ1032/1036 ionization peak is shown on Figure 3-8, indicating its strong T_e dependence. Also the effects of any additional influx of oxygen during the start-up phase are minimized by observing the earlier time signal. Visible lines are available to check the VUV lines. The visible lines OIII λ3763, CIII λ4647, and NIII λ4509 are proportional to the respective VUV lines OIII λ703, CIII λ977, and NIII λ991 at the ionization peak during doping.

Figure 3-7. Ionization peak signals as a function of puffed H concentration for the oxygen ionic states OII through OVI. The signals are normalized to 1.0 at an H concentration of 1.8 X 10^{13} atoms/cm^3. (These plasmas have an electron density of about 1 X 10^{13} cm^{-3}.)

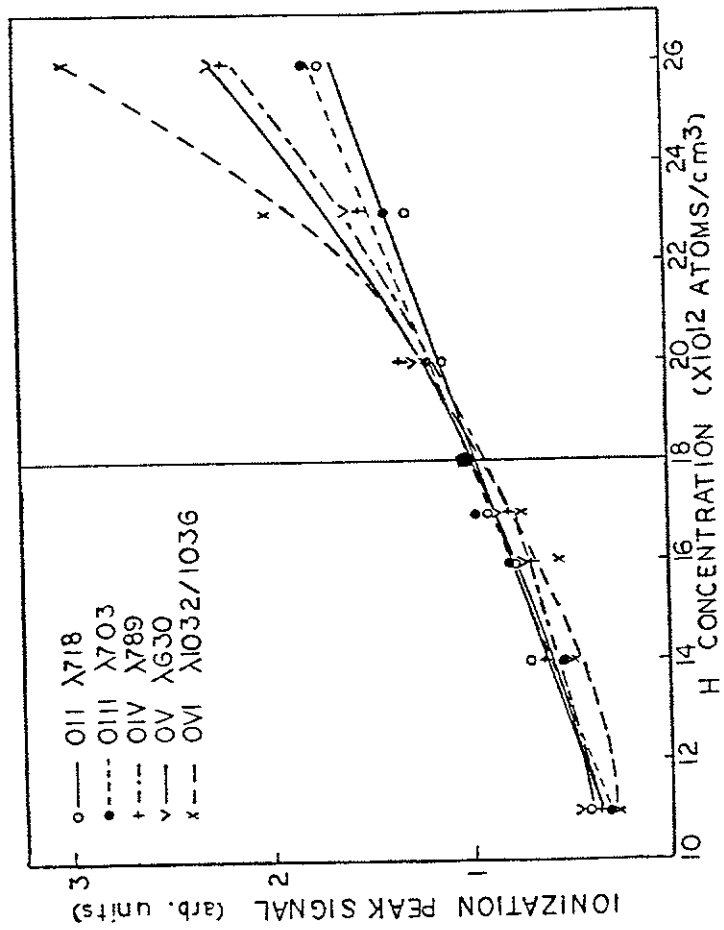

Figure 3-7

Figure 3-8. Ionization peak signals as a function of doped Ar concentration for the oxygen ionic state OII through OVI, taken on the same run as Figure 3-7. The puffed H concentration is 1.8 X 10^{13} atoms/cm^3. For this Figure, two sets of ionization peak times are indicated: for OVI next to the X's, and for OIII next to the solid circles.

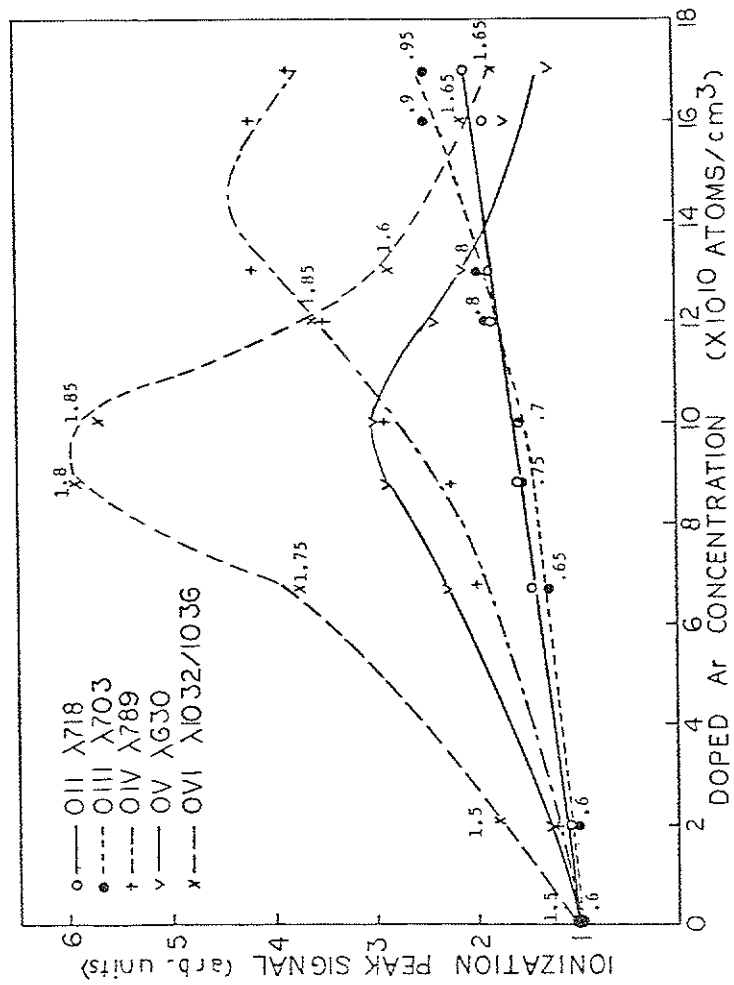

Figure 3-8

Thus, the increase of impurity concentration per dopant atom is roughly proportional to the mass of the dopant. The normalization with respect to the effect of adding hydrogen provides a reference signal for different plasma conditions. The mass variations, shown in Figure 3-9, are similar for OIII, CIII, and NIII. These data summarize the results of the doping series taken (about seven different runs with three to five dopant gas series per run). The error bars thus represent the changes in the mass proportionality factor with changes in machine conditions and plasma parameters. The reproducibility of the impurity production is fortunately quite good. The extent to which the signals represent the impurity concentrations is estimated to be of this same order.

From the mass proportionality shown in these Figures, a momentum transfer process involving the initial plasma ions is implied. Electron- and photon-induced desorption and chemical reactions can play only a minor role in the production of light impurities. The behavior of the plasma ions during start-up is discussed in more detail in the next few chapters.

B. Isotopic Exchange Experiments

In order to estimate the importance of hydrogen-induced desorption relative to intrinsic impurity-induced desorption, we have observed working gas (H_2 and D_2) recycling in studies similar to recycling studies in DITE and other machines.[4,5,6,7,8] This type of experiment has been commonly used to distinguish between the two

Figure 3-9. The relative impurity signal increase for OIII λ703 (a), NIII λ4511 (b), and CIII λ4647 (c) versus the dopant mass (for atoms). The open circles do not represent linear increases (see Section C).

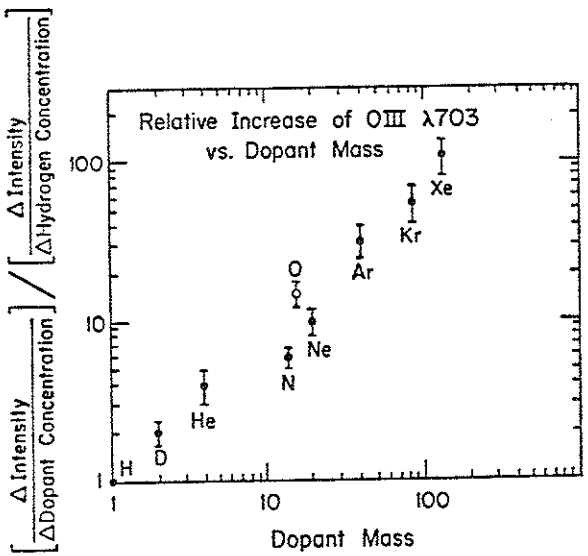

Figure 3-9a

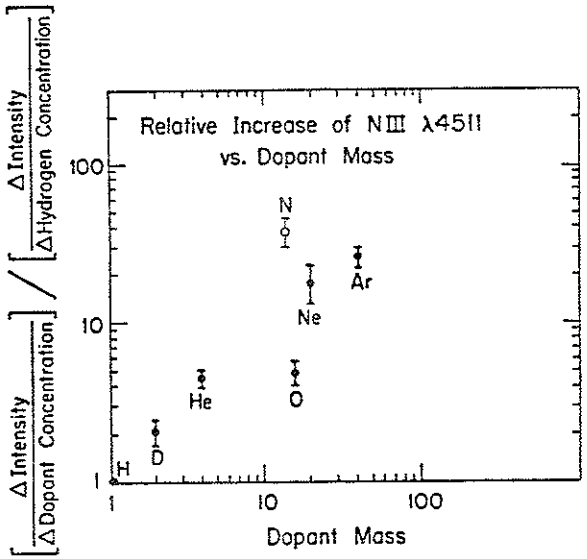

Figure 3-9b

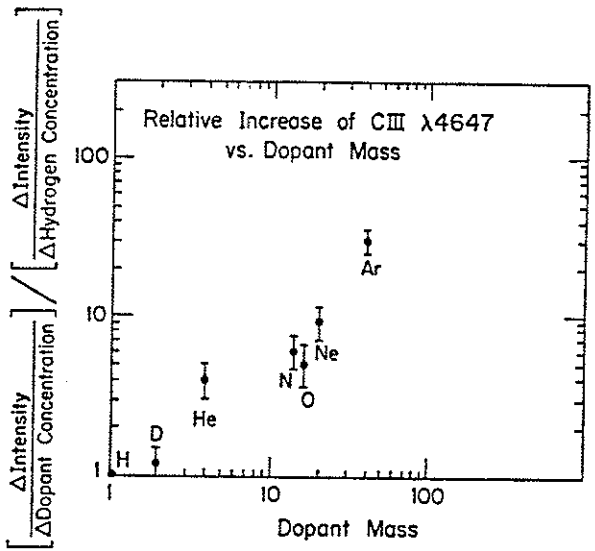

Figure 3-9c

components of the discharge gas, the initially puffed gas and the gas released from the wall. Typically the amount of gas in the tokamak wall is several orders of magnitude larger than the density in the plasma. This gas can diffuse from within the solid to the surface, where it is easily desorbed by the plasma, so that the initially puffed gas can exchange with the wall gas during the course of the discharge. Since the particle confinement time is less than the discharge length this recycling process involves several exchanges with the wall during the course of a discharge. (This description is, of course, oversimplified since tokamaks now generally use additional gas puffing during the discharge to control the recycling process and to keep the density constant. No late gas puffing has been used for these experiments.) The question of particular interest here is the effect of isotopic exchange on impurity levels.

The discharges in Tokapole II had been run almost exclusively in H_2 prior to this experiment. Figure 3-10 shows the change in the plasma constituents after switching the working gas to deuterium. The line radiation signals for H_β and D_β, separated by using slits for 0.3 Å resolution on the visible monochromator, are used to compare the start-up and plateau behavior. For these neutral hydrogen and deuterium lines, the ionization peaks occur at 300 μsec, and the levels are flat by about 500 μsec, so that these signals give a comparison between early and late start-up. The early and late time signals are normalized to be the same for the

Figure 3-10. H_β λ4861 and D_β λ4860 versus number of shots after switching the working gas from H_2 to D_2. The scales for the peaks and plateaus have been normalized to be the same for the first shot. There may be a discrepancy in comparing the intensity of H_β to D_β.

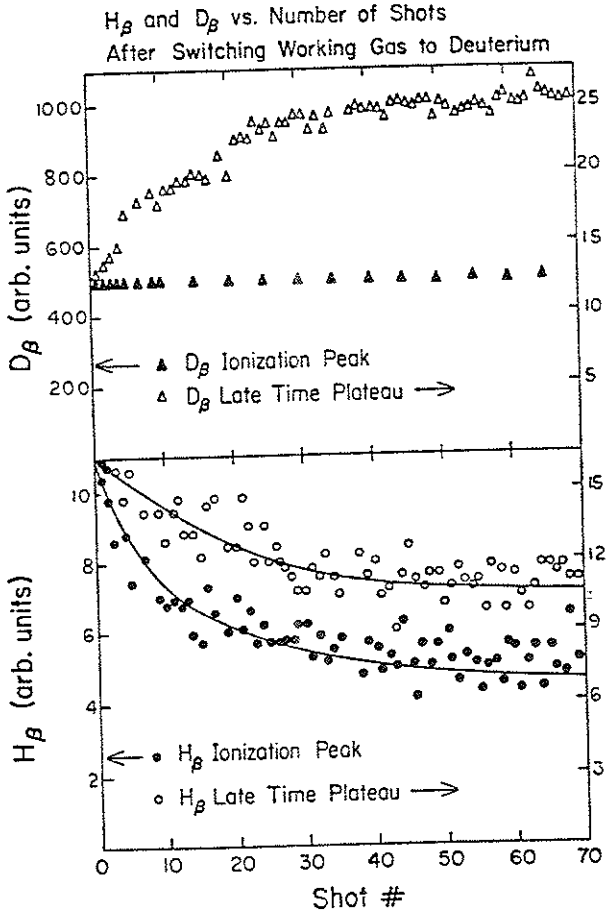

Figure 3-10

first shot. The D_β ionization peak signal is constant during these shots, since, of course, the initial puff is the same throughout these shots and constitutes the dominant discharge gas. The D_β plateau increases gradually to approach a constant level supplied partially from the wall. The hydrogen level in the plasma decreases to approach a constant non-zero level (there is always plenty of H in the system from residual water and hydrocarbons), with the ionization peak decaying somewhat more rapidly. Thus, the initial D plasma has already knocked a substantial amount of H from the wall by 300 μsec. The faster decay of the H_β ionization peak presumably indicates that the most easily desorbed H is replaced by D during the first several shots.

Figure 3-11 shows the effects of switching the working gas back to H_2. The behavior of the wall gas is slightly different from the previous case. For the first several shots the D_β ionization peak and the plateau decay at the same rate; later, the ionization peak begins to decay less rapidly than the plateau. This result seems somewhat inconsistent but may be explained by the difference in the amount of diffusion into the bulk solid between H and D over the short time of D_2 filling and in an environment with residual H_2. The D_β results are reproduced in Figure 3-12 with the additional data from the residual gas analyzer to show the decay of D_2 between shots. The slow decay to zero level is an indication that diffusion of D into the solid has occurred over the short duration of running in D_2.

Figure 3-11. H_β and D_β versus number of shots after switching the working gas back from D_2 to H_2, immediately after the run of Figure 3-10.

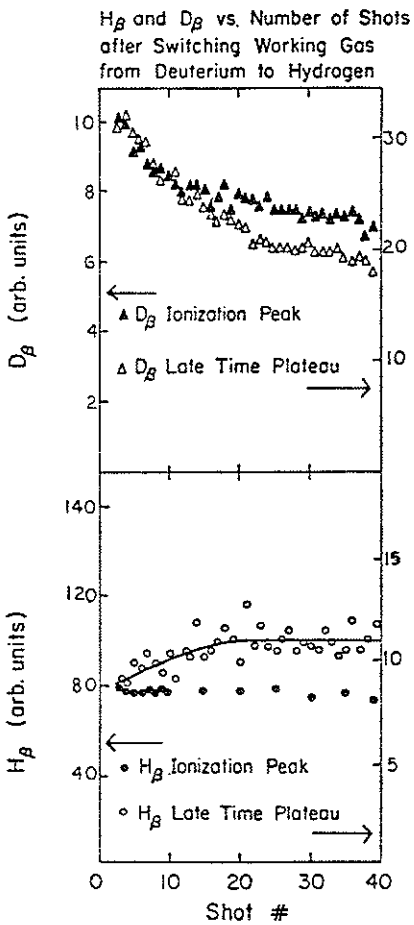

Figure 3-11

Figure 3-12. The D_β results from Figure 3-11 plotted with data from the residual gas analyzer (RGA) between shots.

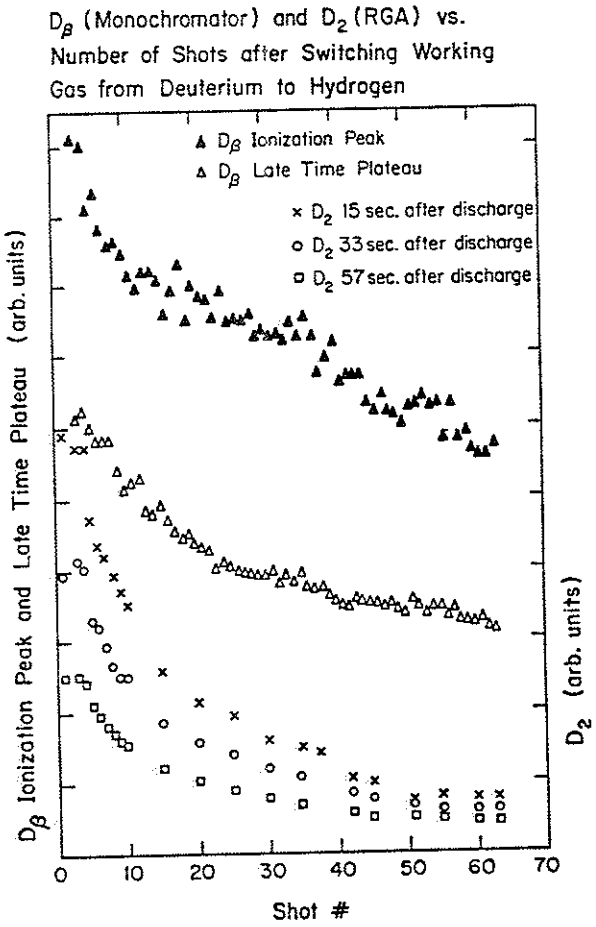

Figure 3-12

For a similar run the OIII λ703 ionization peak shows a dependence on the working gas (Figure 3-13); the late time plateau signal shows no effects for this run. Although this data set is incomplete, the basic results are similar to other observations. After the first several shots the OIII peak has increased by a factor of about 1.4 over its value in H_2. This increase can be explained by the difference in the mass of the working gas as would be consistent with the results of Section A. The smaller increase during the first several shots is probably due to the increase in the ratio of D to H in the very early ($\lesssim$ 200 μsec) plasma shown in Figure 3-10.

If desorption by the intrinsic impurities were dominant over desorption by hydrogen the oxygen effects would be small. The oxygen increase suggests that in an undoped Tokapole plasma, the working gas plays the major role in releasing light impurities. When the machine is dirty or heavily doped, the intrinsic impurities probably play a non-negligible role. More careful modeling of the time-dependence of the influx (Chapter 4) substantiates the conclusion that the plasma formed from the initial puff of working gas (and any dopant gas) has a strong interaction with the wall in the earliest stage of start-up.

Figure 3-13. OIII λ703 versus number of shots after switching the working gas to D_2, with one shot in H_2 after D_2 for a reference level.

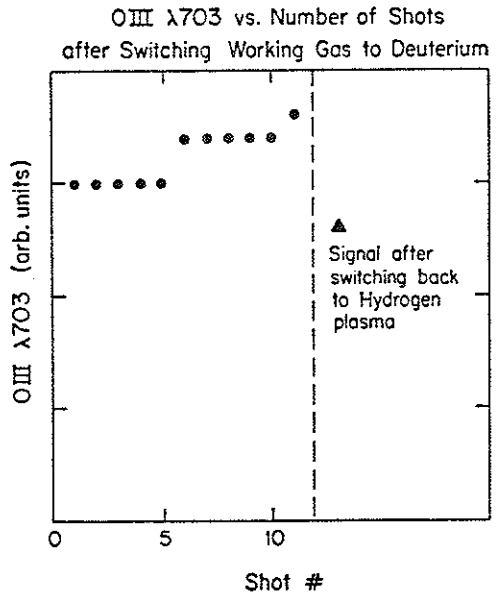

Figure 3-13

C. Intrinsic Impurity Doping Experiments

The understanding of doping experiments which use an intrinsic impurity as the dopant is complicated by the self-desorption process, especially at higher dopant concentrations. The observed impurity increase has two components: the increase of the dopant in the initially puffed working gas, which not only fills the vacuum chamber but also gets pumped by the walls before the discharge starts, and the additional wall impurity desorbed by the higher mass (doped) working gas. (Wall pumping of the dopant from the previous shot has been minimized for all of the data of this thesis by ensuring that the impurity concentration returns to its original level on the first shot after the data run.)

Intrinsic impurity doping has been a useful technique in tokamaks for measuring the absolute impurity concentration in the wall.[3,9] For low dopant concentrations the increase of oxygen with oxygen doping, for example, is linear. The extrapolation of the data points for each ion to zero intensity gives the O concentration in the undoped plasma. The technique may be modified for the effects of self-desorption as shown in Figure 3-14. The line through the data points for OIII λ703 versus doped O concentration has been extrapolated to give 2.0 X 10^{11} O atoms/cm^3. An estimate of the self-desorption is made from comparing data of similar mass impurities: NIII λ991 versus doped O and OIII λ703 versus doped Ne. Subtracting this line gives a corrected line which represents only O

Figure 3-14. Ionization peak signal versus dopant concentration. The X's are data points for OIII λ703 versus O doping through which a straight line (dotted) is drawn, ignoring the nonlinearity beginning at higher doping levels. The extrapolation back to zero doping signal indicates a concentration of 2 X 10^{11} cm^{-3}. A correction is made by subtracting the self-desorption, estimated from NIII λ991 versus O (dashed) and from OIII λ703 versus Ne (dotdashed). The corrected curve (solid) indicates a higher concentration of 2.5 X 10^{11} cm^{-3}.

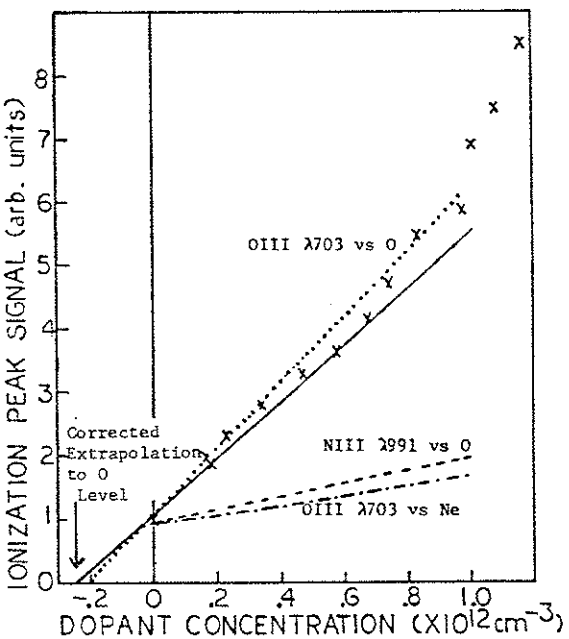

Figure 3-14

added directly to the plasma. This extrapolation gives a slightly higher value of 2.5 X 10^{11} O atoms/cm^3.

The nonlinear response of these experiments provides a useful comparison to the linear response of the experiments in Section A. Figure 3-15 shows the response of CIII, NIII, and OIII to O doping and of NIII and OIII to N doping. In Figure 3-15a the parabolic increase of OIII with doped O clearly occurs for a range of dopant concentration which is linear in NIII and CIII; however, for the same amount of doped N, OIII and NIII are both nonlinear (Figure 3-15b). Since the intrinsic O concentration is a factor of seven times higher than the N concentration, the difference in the nonlinearity must be the consequence of recycling during the discharge. These data are used for the model in Chapter 4 to quantify the recycling during start-up. Qualitatively one can already see in Figure 3-15a that the influx of light impurities must have a strong time dependence. If the plasma recycles several times, gaining effective mass from impurities with each encounter with the wall, all the doping series would be inherently parabolic. The linear response of O to exotic gas doping and the continued linearity of N and C during parabolic O response suggest an early decrease in the recycling rate. (Depletion of the surface contaminants may occur during a shot, but at Tokapole base pressures the Al walls will replenish the surface layer between shots.)

Figure 3-15. Comparisons of impurity response during intrinsic impurity doping, including high dopant concentration levels. The linear response of CIII λ977 and NIII λ991 versus O contrasts the nonlinear response of OIII λ703 versus O (Figure 3-15a) and of NIII λ991 and OIII λ703 versus N (Figure 3-15b).

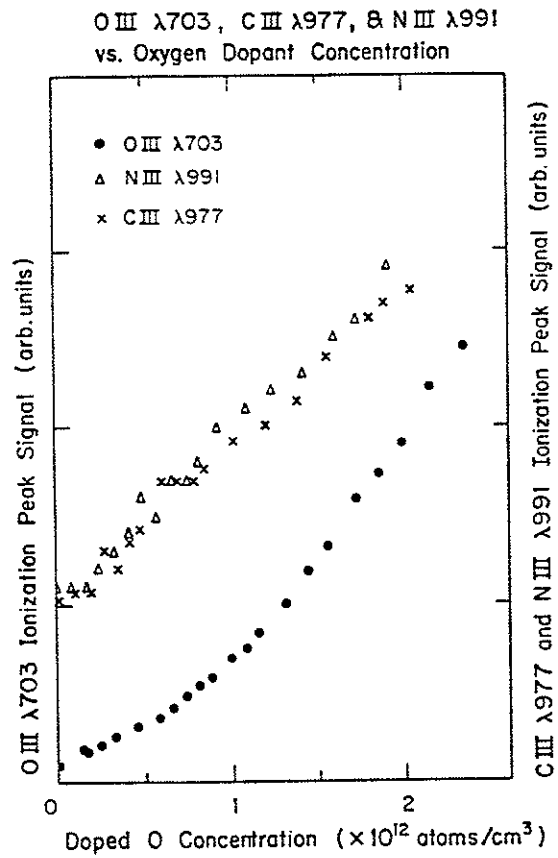

Figure 3-15a

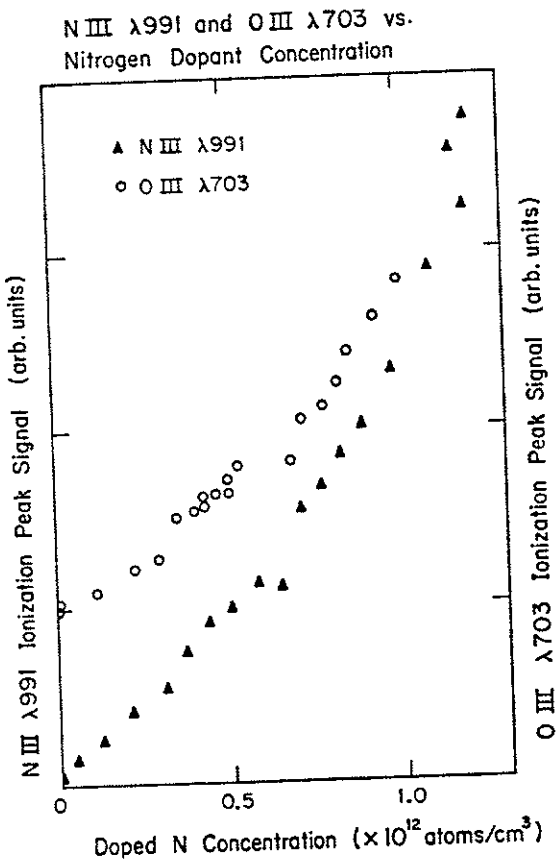

Figure 3-15b

For high enough dopant concentrations all low-Z impurity signals have a nonlinear response. Usually the gross plasma parameters begin to be affected as well, so that the experiments are difficult to interpret. Figure 3-16 shows the effects of high dopant concentrations for the same N data of Figure 3-15b. The parameter $\int I_p dt$ (amp-sec) is used as a figure of merit for the discharge. For the lower dopant levels the discharge length scales with $\int I_p dt$, so that I_p must be relatively constant. Here the increase in radiated power resulting from higher impurity levels probably slows the start-up process by consuming volt-sec. For higher dopant concentrations the current is lowered as well and the general plasma behavior deteriorates.

Figure 3-16. NIII λ991 and $\int I_p dt$ versus doped N concentration, showing the degradation of the plasma for high doping levels.

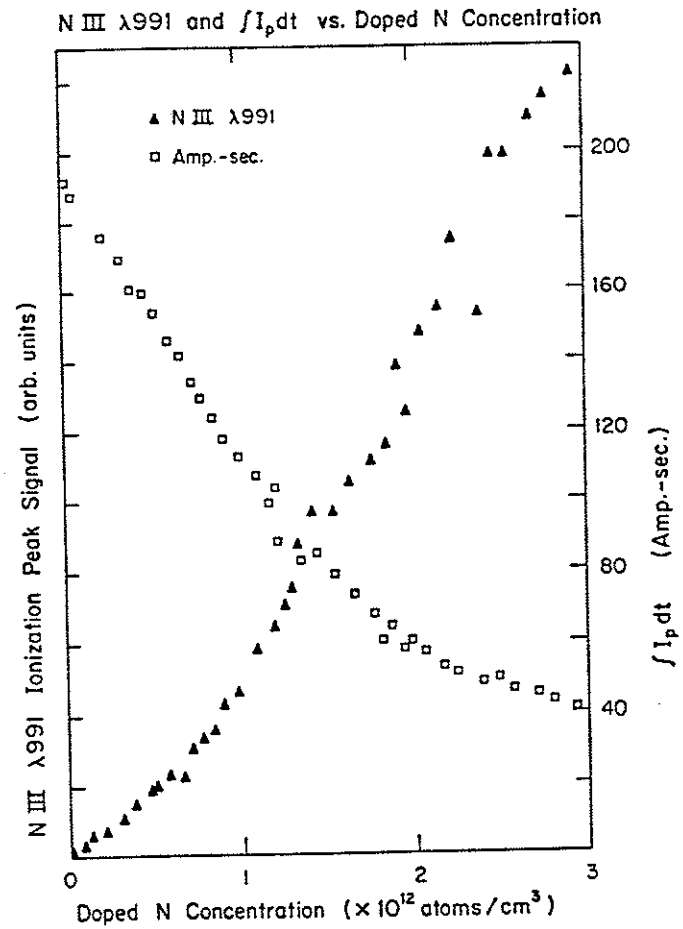

Figure 3-16

REFERENCES

[1]G. Lewin, Fundamentals of Vacuum Science and Technology, McGraw Hill, New York (1965).

[2]S. Dushman, Scientific Foundations of Vacuum Technique, 2nd ed., Wiley, New York (1962).

[3]R.J. Groebner, Ph. D. Thesis, University of Wisconsin (1979).

[4]G.M. McCracken, S.J. Fielding, S.K. Erents, A. Pospieszczyk, P.E. Stott, Nucl. Fusion 18 (1978) 35.

[5]S.J. Fielding and A.D. Sanderson, J. Nucl. Mater. 93/94 (1980) 220.

[6]H.C. Howe, J. Nucl. Mater. 93/94 (1980) 17.

[7]T.F.R. Group, J. Nucl. Mater. 111/112 (1982) 199.

[8]R.J. Groebner, University of Wisconsin Plasma Studies PLP 742 (1978).

[9]L. Oren and R.J. Taylor, Nucl. Fusion 17 (1977) 1143.

CHAPTER 4

ION-INDUCED DESORPTION DURING START-UP -- MODEL

A simple model of working gas and impurity recycling describes the major effects of the early-time doping experiments on Tokapole II. This model is consistent with the observed linearity of impurity increases with doping and the experimental observations of the time development of the oxygen series line radiation. The calculation uses a time-dependent coronal equilibrium rate equation for oxygen ionization and recombination[1,2] to find the influx term. A computer code solves for the emissivities of the ionizing oxygen states given $T_e(t)$, $n_e(t)$, the particle confinement time τ, all experimentally observable in principle, and an influx term, to be determined.

A. The Time-Dependent Coronal Model[2,3]

For a plasma in thermodynamic equilibrium, particle collision processes determine the population densities of the electrons in the various energy levels and in different ionic states. These population densities are given by the Boltzmann equation,

$$\frac{n_z^p}{n_z^q} = \frac{\omega_z^p}{\omega_z^q} \exp\left(\frac{\varepsilon^{p,q}}{kT_e}\right) \qquad (4\text{-}1)$$